Optimal Operational Planning of Scalable DC Microgrid with Demand Response, Islanding, and Battery Degradation Cost Considerations

Muhammad Fahad Zia[a], Elhoussin Elbouchikhi[b], Mohamed Benbouzid[a,c]

[a]University of Brest, UMR CNRS 6027 IRDL, 29238 Brest, France
[b]ISEN Brest, Yncréa Ouest, UMR CNRS 6027 IRDL, 29200 Brest, France
[c]Shanghai Maritime University, 201306 Shanghai, China

Abstract

With the advancements in power electronic devices, the increasing use of DC loads, DC renewable generation sources and battery storage systems, and no reactive power and frequency stability issues, DC microgrids are increasingly gaining attention in both academia and industry. In this paper, a grid-connected DC microgrid is considered, which consists of a PV system and a Li-ion battery. DC microgrids optimal operation requires battery degradation cost modeling and demand response incentive for active consumers' participation to be addressed in detail. Therefore, a practical degradation cost model for a Li-ion battery is developed to optimize battery scheduling and achieve its realistic operational cost. Apart from energy price, scheduled islanding responsive demand response incentive is also introduced to encourage customers to shift load during scheduled grid-tie line maintenance. Levelized cost of energy of PV system is calculated for both hot and cold climate regions. Optimal operation of DC microgrid cannot be achieved without considering nodal voltages and system losses. Hence, network constraints are also included in the proposed model. Extensive numerical simulations are carried out to prove the effectiveness of the proposed approach. The achieved results would aid in DC microgrids adoption planning that would expectedly replace traditional AC grids in the future.

Keywords: **DC microgrid, photovoltaic system, Li-ion battery, battery degradation cost model, demand response, energy management system, optimization.**

Nomenclature

χ_d^{Υ}	Depth of discharge dependent battery cyclelife factor.
χ_T^{Υ}	Temperature dependent battery cyclelife factor.
χ_T^{Ξ}	Temperature dependent battery capacity factor.
Δt	Time interval.
$\delta_1, \delta_2, \delta_3$	Time-of-use based scaling factors for demand response incentives.
η^{ch}	Charging efficiency of battery.
η^{dch}	Discharging efficiency of battery.
$\mathcal{N}_\mathcal{V}, \mathcal{N}_\mathcal{W}, \mathcal{N}_\mathcal{X}$	Sets of PV, battery, and load buses.
$\mathcal{N}$	Set of all buses including grid bus.
$\mathcal{T}_1, \mathcal{T}_2, \mathcal{T}_3, \mathcal{T}$	Sets of off-peak, mid-peak, on-peak, and all time slots.
$\mathcal{T}_{sh}$	Set of forward and backward shifting time instants.
Φ	Chemical reaction rate of Li-ion battery.
Φ_{ref}	Chemical reaction rate of Li-ion battery at reference temperature.
π_t^{dr}	Demand response incentive price at time t.
π_t^{g+}, π_t^{g-}	Buying and selling electricity prices at time t.
ρ_1, ρ_2, ρ_3	Schedlued islanding sensitive scaling factors for demand response incentives.
σ	PV system degradation factor.
$\Upsilon_{w,ref}$	Reference cyclelife of Li-ion battery at battery bus w.
$\Xi_{w,ref}$	Rated energy capacity of Li-ion battery at battery bus w.
$\Xi_{w,t}$	Li-ion battery energy capacity at battery bus w and time t.
C^b, C_{inv}^b, C_{om}^b	Battery degradation, investment, and operation and maintenance costs.
C_{inv}^b	Investment cost of battery.
$C^{pv}, C_{inv}^{pv}, C_{om}^{pv}$	Levelized cost, investment cost, and operation and maintenance cost of PV system.
C^{voll}	Value of lost load.
CR_{max}	Maximum charging (discharging) rate limit of Li-ion battery.
d	Depth of discharge of Li-ion battery.
dr	Discount rate.
E_{an}^{pv}	Annual energy produced by PV system.
$E_a(\Phi)$	Activation energy.
G_t	Irradiance at time t.
G_{NOCT}	Irradiance at PV array nominal operating cell temperature.
G_{STC}	Irradiance at PV array standard test conditions.
$h_\Upsilon(d), h_\Upsilon(T)$	Regression model for battery cyclelife depen-

	dence on depth of discharge and temperature.
$h_\Xi(T)$	Regression model for battery capacity dependence on temperature.
L_{ref}^b	battery cyclelife at reference conditions.
L_t^b	Baseline power demand at time t.
N^{pv}	Number of PV arrays.
$NOCT$	Nominal operating cell temperature.
P_t^i	Active power at bus i during time t.
$P_{w,t}^{ch}$	Charging power of battery at battery bus w and time t.
$P_{w,t}^{dch}$	Discharging power of battery at battery bus w and time t.
$P_{x,t}^{dr+}$	Power demand at load bus x shifted from time t.
$P_{x,t}^{dr-}$	Power demand at load bus x shifted at time t.
$P_{i,t}^{DR}$	Maximum shiftable power demand from period t.
$P_{x,i,t}^{dr}$	Power demand at bus x shifted from time slot i to t.
P_t^{g+}, P_t^{g-}	Buying and selling power from/to grid power at time t.
P_t^{loss}	Power loss of the DC microgrid system at time t.
$P_{ij,t}^{loss}$	line loss of branch connected between bus i and bus j.
$P_{x,t}^{ls}$	Power demand of lost load at load bus x and time t.
P_t^l	Power demand at time t after shifting.
P_{STC}^{pv}	PV array power output at standard test conditions.
$P_{v,t}^{pv}$	Power output of PV system at PV bus v and time t.
R	Gas constant.
$R_{w,t}^{ch}$	Charging rate of Li-ion battery at battery bus w and time t.
$R_{w,t}^{dch}$	Discharging rate of Li-ion battery at battery bus w and time t.
RV	Residual value of Li-ion battery.
T	Ambient temperature.
t	Indices of time slots.
t_f	End time.
t_s	Start time.
T_c	Cell temperature of PV array.
T_{ref}	Reference temperature.
T_{STC}	Cell temperature of PV array at standard test conditions.
v, w, x	Indices of PV, battery, and load buses.
V_t^i	Voltage at bus i during time t.
V_{max}^i	Maximum limit of bus voltage.
V_{min}^i	Minimum limit of bus voltage.
y_{ij}	Line admittance from bus i to bus j.
z_t	Islanding status at time t.

1. Introduction

Renewable energy sources (RESs) are being deployed on a large scale due to the advancement and maturity in their tech-nologies. Among these sources, photovoltaic (PV) systems are leading in terms of installation and utilization followed by wind turbines. Integration of these sources along with energy storage systems paves the way for microgrids (MGs) [1]. An MG integrates all such distributed energy sources with plug and play ability to operate in islanded mode during maintenance or failure of grid-tie line [2]. MGs reduce burden on aging transmission network by meeting load demand locally with the help of distributed energy sources connected to local substation and distribution networks [3, 4].

MGs can be either AC or DC, and hybrid depending upon the type of buses, loads, and RESs [5, 6]. Although, current utility grid (UG) system is of AC type, DC loads such as lightening systems, computers, and battery chargers are significantly increasing [7]. Recent advancements in power electronic devices also pave the way for modeling loads as constant power loads due to negligible effects of transient behavior in output power of many loads [8]. Moreover, quite a few RESs produce DC voltages, thus requiring power converters for AC conversion that reduces efficiency of the overall system. DC MGs are less complex power systems with the advantages of no reactive power flow and no complex control circuitry for frequency stability as well [9]. DC MGs can operate in grid-connected and islanded modes.

The battery storage system plays a vital role in an MG as it can be used in various applications such as peak demand management, uncertainties handling caused by RESs, and providing supply to load end during islanding operation [10, 11]. In DC MG operation, battery continuously charges and discharges, which affects its performance and cyclelife. Hence, a practical model of battery degradation cost (BDC) is necessary to optimize its scheduling during DC MG operation. Battery performance is affected by charge (discharge) rate, depth of discharge (DOD), state of charge (SOC), and temperature. Therefore, BDC should be modeled considering all these parameters. Such BDC model avoids higher costs for the DC MG operator (DMO) due to imprudent charging and discharging times.

Researches have proposed various BDC models for battery scheduling optimization and overall system operation. An economic operation of a PV/battery system with a basic BDC model was proposed in [12]. However, the BDC model has not included explicit consideration of battery aging factors, thus providing inefficient cost-competitive model. In [13], a PV/battery system has scheduled its decision strategies using operating cost model that considers only capacity fading effects in modeling BDC. Moreover, battery degradation model was used in energy management of remote MGs in [14]. The degradation model considers DOD effects on battery lifetime only. The other battery aging factors are not taken into consideration. In [15], an optimized management of PV integrated off-grid power system was achieved. MG energy scheduling was achieved by using only DOD-dependent BDC model in operational cost-function of MG [16]. The BDC model was developed by considering only lifetime energy throughput of battery and ignoring other aging factors.

A grid-connected PV/battery system operation was proposed in [17]. In this study, DOD-dependent battery cyclelife degra-

dation model estimates battery sizing. However, the daily rule-based operation neglects battery degradation in deciding strategies for efficient PV/battery system operation. Rule and model predictive-based control techniques were used to minimize the operating cost of PV/battery system in [18]. The developed model includes capacity loss degradation in battery operation that considers only SOC-based aging effects. Moreover, the degradation cost of battery is hypothetically assumed. Authors in [19] have proposed battery aging model for MG optimal design. The degradation model is developed based on capacity loss of battery that considers capacity fading only. Moreover, the capacity loss is taken constant for a range of temperature without providing reference of any manufacturers datasheet. Operating cost of RESs-based MG is optimized in [20]. Authors have considered only the DOD related aging effects in BDC modeling, which does not provide the practical degradation model for batteries. All these battery degradation models only consider capacity fading of battery, while ignoring power fading. Capacity fading is related to cyclelife degradation of battery and power fading is related to ohmic and reaction losses, which is connected to energy (discharged) capacity degradation of battery. Optimal operation of battery in a DC MG is a complex problem due to its intertemporal nature. Lead acid and Li-ion batteries are the most widely used energy storage systems in energy management applications. Nowadays, Li-ion batteries are dominating due to their high energy density, no memory effect, and increased resistance to temperature effects. They are being deployed at large scale for utility, regulation, and electric vehicle (EV) applications [21]. In 2017, annual deployment of Li-ion batteries was 2 GWh, and it is predicted to go up to 18 GWh in 2022 [22]. In this paper, BDC of a Li-ion battery is modeled to optimize the overall operation of a DC MG.

Demand response (DR) is becoming an integral part of power system and MGs due to its applications in minimizing system operational cost [23], congestion management [24], peak demand management [25], defer investment in power network [26], system reliability [27], and ancillary services [28]. DR operation is achieved by utilizing smart meters, advanced metering infrastructure, and energy information systems. An advanced metering infrastructure is used to collect data from metering devices using home area network. These data log are sent to service provider by wide area network for analysis in order to achieve energy cost and consumer service optimization [29].

DR is divided mainly into two types, price-based DR (PDR) and incentive-based DR (IDR). PDR programs help the consumers to change their consumption pattern with time-varying energy prices. However, IDR programs provide benefits to consumers for reducing their load demand following DR requests. Most utilities provides PDR programs to their consumers instead of IDR, but PDR shares a small contribution in overall DR resource base [30]. IDR provides great provision and control to DMO, which enables performing efficient MG operation. In this paper, IDR is used for optimal and efficient operation of a DC MG.

A generalized PV and battery-based grid-connected DC MG model is presented in Fig. 1. PV system, and DC and AC loads are connected to the DC network through DC/DC converters
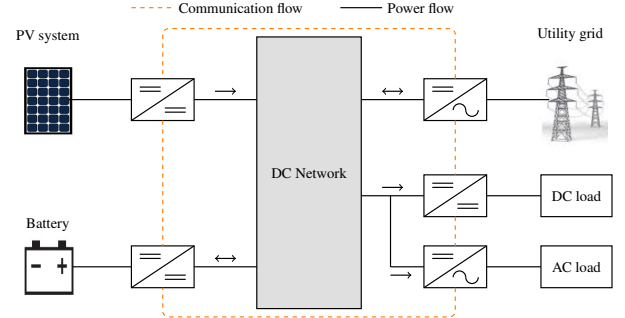

Figure 1: DC MG architecture.

and inverters, respectively. A bidirectional DC/DC converter is used to control power flow between Li-ion battery and DC network during charging and discharge. In grid-connected mode, a DC MG can reap advantages of selling power to UG during excess supply period and the bidirectional DC/AC converter is used for this purpose. While in islanded mode, it provides supply to loads through local sources. All the energy sources, loads, and UG local controllers communicate with each other and DMO using communication technologies. These wired and wireless technologies are selected based on the criteria of deployment cost, coverage area, and data rate [1]. Power output of the PV system is used at first to meet load demand followed by UG power and battery power. DMO needs centralized decision-making strategies to avoid ineffective and costly operation of the DC MG. Therefore, optimized daily scheduling of energy sources in a DC MG requires an energy management model to minimize its operating cost and optimize its daily operation.

In this paper, optimal operation of a scalable PV and Li-ion battery based grid-connected DC MG is studied considering scheduled islanding and time-of-use (TOU) based IDR schemes. The BDC model of Li-ion battery is developed taking into account the effects of temperature and DOD on battery performance. The levelized cost of energy (LCOE) of the PV system is determined using real data of temperature and irradiance of hot and cold weather climate regions, namely Dammam (Saudi Arabia) and Brest (France), respectively. The proposed cost-operation model of a scalable grid-connected DC MG is a nonlinear programming model that also considers bus voltages and includes system losses in power balance constraint. The contributions of this paper can be summarized as follows:

- Regression models are developed to determine temperature and DOD effects on cyclelife and energy capacity degradation of a Li-ion battery.

- A practical BDC model of Li-ion battery is presented using the developed regression models.

- A practical LCOE of a PV system for hot and cold climate regions is computed using real temperature and irradiance data.

- An IDR is introduced to encourage customers to change their consumption patterns during normal operation.

- An islanding responsive IDR is proposed to encourage customers to shift load from scheduled islanding periods to normal operation periods.

- Power flow of a scalable DC MG system is also included in the optimization model to regulate bus voltages and compute system losses.

2. Battery Degradation Modeling

Li-ion battery energy storage systems are an essential part of MGs due to their high power and energy densities, good cyclelife, and improved efficiency. They are being widely used in energy systems for various applications such as bulk storage, peak shaving, frequency regulation, voltage support, reserve capacity, and transmission and distribution deferral [31]. Nowadays, Li-ion batteries are the most mature and commercial technologies used in power system. However, integration of Li-ion battery into an MG system requires its degradation cost-modeling for effective and efficient operation.

Increasing cell impedance and decreasing battery capacity due to unwanted side reactions lead to fast degradation of battery [32, 33]. Hence, the battery chemistry and its scheduling operation plays a major role in affecting battery cyclelife. The most important parameters in battery degradation are energy capacity and cyclelife. These parameters depend on temperature, depth of discharge (DOD), state of charge (SOC), charge and discharge rates (c-rate), battery application, type of battery, and battery manufacturer. However, battery degradation modeling becomes unrealized as the effects of these degradation factors cannot be analyzed and modeled individually. Therefore, the most important degradation factors are considered to be temperature, DOD, SOC, and c-rate. Several studies have shown that SOC can also be defined in the form of a DOD. A battery with DOD of d completes its charge-discharge cycle by discharging from 100% SOC to $(100 - d)$% SOC and then charging back to 100% SOC [34].

Li-ion battery manufacturers' datasheets show that the value of c-rate below 1 does not affect the energy capacity. However, when increasing the c-rate above 1, the energy capacity of a Li-ion battery starts decreasing [35, 36]. The charge and discharge rate limits of a high energy capacity Li-ion battery storage system do not go beyond 0.5, which is discussed in [37], based on technical investigations. Therefore, the c-rate effect on battery degradation modeling is ignored. Moreover, effects of charge and discharges rate on battery cyclelife is negligible and it can be ignored too [38, 39]. Hence, a BDC model is proposed considering the effects of temperature and DOD on its energy capacity and cyclelife.

2.1. Temperature

Temperature affects the chemical reaction rate of Li-ion battery, thus affecting its capacity. Arrhenius equation describes the increasing exponential dependence of reaction rate on temperature. Therefore, battery capacity increases with temperature due to increase in its chemical reaction rates. This increase in battery capacity means that the battery can provide more power at high temperatures. Arrhenius effect is expressed as [40]:

$$\Phi = \Phi_{ref} \left[\frac{E_a(\Phi)}{R} \left(\frac{1}{T_{ref}} - \frac{1}{T} \right) \right] \tag{1}$$

The regression model for temperature dependent battery energy capacity relation is determined using the data from Li-ion battery data-sheet as shown in Fig. 2 [35]. The battery loses capacity to provide the same power at low temperatures due to metallic Lithium plating that causes electrolyte decomposition [41]. Equation (2) describes the relation between battery capacity and temperature.

$$h_\Xi(T) = \alpha e^{-\beta T} + c \tag{2}$$

where $\alpha = -0.354, \beta = 0.0310$, and $c = 1.157$.

Li-ion battery usage at very high temperatures results in severely decreasing the cyclelife. This is caused by higher solid electrolyte interphase film accumulation, thus causing faster decay in cyclelife and increasing battery aging process [42, 43]. The graphical relation between cyclelife and temperature provided in [34] and shown in Fig. 3, can be modeled as:

$$h_\Upsilon(T) = \begin{cases} \alpha_1 e^{-\beta_1 T} + \gamma_1, & -40°C \leq T < 0°C \\ \alpha_2 T + \beta_2, & 0°C \leq T < 18°C \\ \alpha_3 T + \beta_3, & 18°C \leq T < 50°C \\ \alpha_4 e^{-\beta_4(T-50)} + \gamma_4, & 50°C \leq T \leq 80°C \end{cases} \tag{3}$$

where $\alpha_1, \alpha_2, \alpha_3, \alpha_4, \beta_1, \beta_2, \beta_3, \beta_4, \gamma_1, \gamma_4$ are the parameters of the aforementioned model that provide best fit to the experimental data. $\alpha_1 = -3050.056, \beta_1 = 0.023, \gamma_1 = 7811.54, \alpha_2 = 14.964, \beta_2 = 4767.474$ in this study. Similarly, $\alpha_3 = -6.99, \beta_3 = 5169.082, \alpha_4 = -149.889, \beta_4 = 0.117, \gamma_4 = 4981.68$.

2.2. Depth of Discharge

Theoretically, DOD is defined as the absolute discharge relative to the related battery capacity. It is represented as SOC
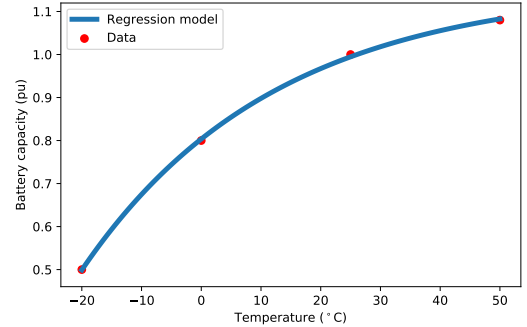

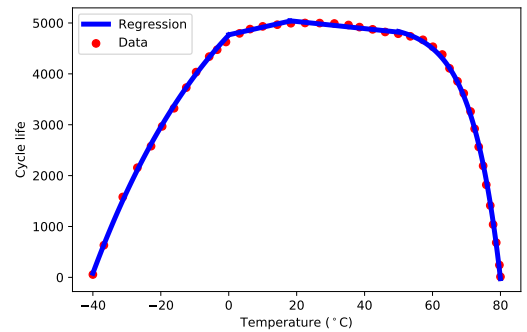Figure 2: Effect of temperature on Li-ion battery capacity.

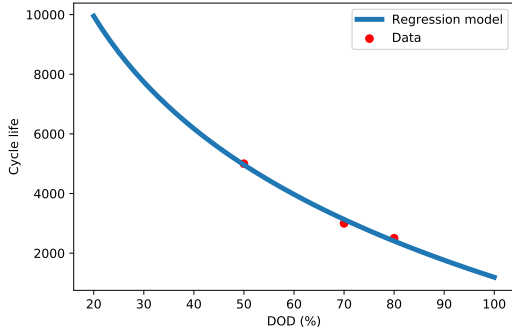Figure 3: Effect of temperature on Li-ion battery cyclelife at 50% DOD.

Figure 4: Regression curve of Li-ion battery cyclelife vs DOD.

subtracted from 100% charge $(1 - SOC)$. DOD has a minimal effect on battery power fading [44] and is ignored in power fading modeling. However, DOD causes mechanical stresses and side reactions in battery, which result in decreasing its cyclelife. Therefore, cyclelife is strongly dependent on DOD. The higher the DOD is, the lesser battery cyclelife will be. A relation between cyclelife and DOD of a Li-ion battery is obtained using practical results taken from [35], as presented in Fig. 4. Equation (4) presents the logarithmic model that describes the effects of DOD on a battery cyclelife.

$$h_\Upsilon(d) = \alpha \log(d) + \beta \qquad (4)$$

where d represents DOD of Li-ion battery. α and β are regression coefficients of cyclelife dependence on DOD. In this case, $\alpha = -5440.35$ and $\beta = 1191.54$.

2.3. Battery Degradation Cost

Several studies have proposed various battery degradation cost models incorporating mainly DOD and temperature effects. However, temperature effects are only considered in determining cyclelife or capacity fading of battery. In this paper, power fading due to temperature change is also performed by considering its effects on battery capacity. The effect of temperature on battery capacity is defined as the ratio of Ξ_T to Ξ_{ref}, as presented in (5).

$$\chi_T^\Xi = \frac{\Xi_T}{\Xi_{ref}} \qquad (5)$$

Similarly, the effects of temperature and DOD on cyclelife are also defined as Υ_T to Υ_{ref} and Υ_d to Υ_{ref}, respectively. Equations (6) and (7) describe these two factors.

$$\chi_T^\Upsilon = \frac{\Upsilon_T}{\Upsilon_{ref}} \qquad (6)$$

$$\chi_d^\Upsilon = \frac{\Upsilon_d}{\Upsilon_{ref}} \qquad (7)$$

In respect of consideration of temperature and DOD, the BDC of a Li-ion battery, C^b, can be calculated using Eq. (8). A factor of $\frac{1}{2}$ is used to account for both charge and discharge actions during a cycle. The residual value (RV) is defined as economic value of the Li-ion battery at the end of its useful life. The proposed BDC model is developed based on engineering economic principles [45]. The BDC model computes present values of RV and annual operation and maintenance costs of the Li-ion battery with a discount rate dr and a lifetime of n years.

$$C^b = \frac{1}{2} \frac{\left[C_{inv}^b + \sum_{i=1}^{n} C_{om}^b (1 + dr)^{-i} \right] (1 + dr)^n - RV}{(1 + dr)^n \chi_T^\Xi \chi_T^\Upsilon \chi_d^\Upsilon \Upsilon_{ref} \Xi_{ref}} \qquad (8)$$

3. PV System Cost Modeling

A need for distribution generation, energy supply to remote areas, and maturity in technology development pave the way for large deployment of PV systems worldwide. The overall global deployment status of PV systems is 385.6 GW until 2017, among which China, Japan, Germany, and USA are major contributors with the installation of 130.6 GW, 48.6 GW, 42.4 GW, and 41.1 GW of PV systems, respectively [46]. External factors, such as solar irradiance, temperature, and geographical location, affect the power generation output of PV systems. In this paper, the estimated power output of a PV system, with standard test conditions (STC) and nominal operating cell temperature (NOCT) conditions, is calculated as [47]:

$$P^{pv} = N^{pv} P_{STC}^{pv} \left[\frac{G}{G_{STC}} \{ 1 - \gamma (T_c - T_{STC}) \} \right] \qquad (9)$$

$$T_c = T + \frac{G}{G_{NOCT}} (NOCT - 20) \qquad (10)$$

LCOE is a widely used metric to determine the electricity generation cost of various energy technologies over the system lifespan. Therefore, electricity production cost of a PV system is calculated based on LCOE. The investment cost of PV system includes capital cost of module and converters, labour installation cost, construction cost, land acquisition cost, and other hardware balance of system cost. Based on engineering economic principles, Eq. (11) can be used to calculate the PV system LCOE, C^{pv}, [48]. The energy output of the PV system is determined by averaging solar power over a time interval of one hour and summing it up all to get E_{an}^{pv}. The present values of C_{om}^{pv} and E_{an}^{pv} are computed each year with a dr over system life of n years. As PV system performance decreases with time, degradation factor, σ, is associated with E_{an}^{pv} after first year.

$$C^{pv} = \frac{C_{inv}^{pv} + \sum_{i=1}^{n} C_{om}^{pv} (1 + dr)^{-i}}{\sum_{i=1}^{n} E_{an}^{pv} (1 - \sigma)^{i-1} (1 + dr)^{-i}} \qquad (11)$$

The degradation in PV energy output is accounted to start from second year. Degradation occurs due to oxidation, thermal stresses, degradation of interconnections, weather effects, and microscopic cracks [49].

4. Incentive-based Demand Response Modeling

DMO uses IDR in the proposed model as consumers give control access to DMO for shiftable load entities and receive incentives for it in return. Therefore, DMO can adjust the shiftable loads to off-peak periods, less generation supply periods, and scheduled islanding periods, while satisfying system constraints.
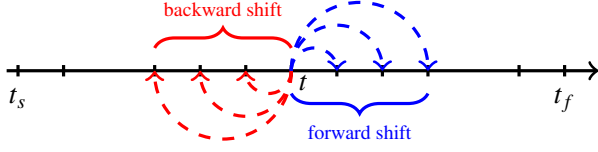
5

Figure 5: DR mechanism.

There are many types of shiftable loads that can be used in DR. Heating, ventilation, and air conditioning (HVAC), dishwasher, electric water heater, electric vehicle, and lightning are few examples. However, integration of these shiftable loads in the DC MG energy management model makes the problem non-convergent and requires higher computational time. Therefore, DMO aggregates shiftable load demand for each time t that helps in solving the developed model efficiently.

Consumers provide information to DMO about quantity and shiftable duration of their deferrable loads. These loads can be shifted backward, forward, or both. It is assumed that these informations are available to DMO. The process flow of DR mechanism with forward and backward shift time instants is shown in Fig. 5. The forward and backward shift instants can be consecutive or non-consecutive. They should remain between final time, t_f, and start time, t_s. Moreover, the cardinality of set of shiftable time instants, $\mathcal{T}_{sh}$, should be less than the total simulation time, as presented in (12). The cardinality refers to the size of a set.

$$|\mathcal{T}_{sh}| \leq t_f - t_s \tag{12}$$

DMO offers IDR to customers to participate in DR during normal and scheduled islanding periods. Scheduled islanding responsive IDR is introduced to encourage customers to shift load to normal operation period. It results in reducing lost load during scheduled islanding period. The IDR model is provided in (13).

$$\pi_t^{dr} = \begin{cases} (\delta_1 + \rho_1 z_t)\pi_t^{g+}, & t \in \mathcal{T}_1 \\ (\delta_2 + \rho_2 z_t)\pi_t^{g+}, & t \in \mathcal{T}_2 \\ (\delta_3 + \rho_3 z_t)\pi_t^{g+}, & t \in \mathcal{T}_3 \end{cases} \quad \mathcal{T}_1 \cup \mathcal{T}_2 \cup \mathcal{T}_3 = \mathcal{T} \tag{13}$$

IDR scaling factors are defined in range of $0 \leq \delta_1, \delta_2, \delta_3 < 1$ for off-peak, mid-peak, and on-peak periods, respectively. Similarly, scheduled islanding responsive IDR scaling parameters are also defined in the same range of $0 \leq \rho_1, \rho_2, \rho_3 < 1$. $\mathcal{T}_1, \mathcal{T}_2$, and $\mathcal{T}_3$ are sets of off-peak, mid-peak, and on-peak energy price time instants, respectively.

5. Energy Management Model

It is considered a grid-connected scalable DC MG consisting of a PV system, a Li-ion battery storage system, and shiftable and critical load demand. The proposed energy management model considers battery degradation model, DR, network power flow, and pre-determined islanding duration to optimize its optimal energy management operation while satisfying technical constraints. A centralized optimal operation is achieved by considering a central controller, DMO, that collects all the neccessary information and optimizes the day-ahead energy management operation over a 24h time horizon $\mathcal{T} := \{t_s, t_s + \Delta t, t_s + $

$2\Delta t, ..., t_f\}$. Detail of the energy management model are described in the following.

5.1. Objective Function

The objective of DMO is to ensure the optimal operation of the microgrid by minimizing its operating cost. The objective function considers energy trading cost with UG, LCOE of a PV system, battery degradation cost, load shedding cost, and DR incentive cost. Equation (14) presents the cost-function of DMO. As discussed in section II, BDC for each battery w and time t is described in (15). Selling energy price from DMO side is considered to be $\pi_t^{g-} = \lambda \pi_t^{g+}$, where λ should be $0 \leq \lambda < 1$. It is assumed that buying, selling, and DR incentive prices are defined with order $\pi_t^{dr} < \pi_t^{g-} < \pi_t^{g+}$ for any $t \in \mathcal{T}$.

$$\begin{aligned} \min \sum_{t=t_s}^{t_f} & \left\{ (\pi_t^{g+} P_t^{g+} - \pi_t^{g-} P_t^{g-}) + \sum_{v \in \mathcal{N}_V} C^{pv} P_{v,t}^{pv} \right. \\ & + \sum_{w \in \mathcal{N}_W} C_{w,t}^b \left(\eta^{ch} P_{w,t}^{ch} + \frac{P_{w,t}^{dch}}{\eta^{dch}} \right) \\ & \left. + \sum_{x \in \mathcal{N}_X} (C^{voll} P_{x,t}^{ls} + \pi_t^{dr} P_{x,t}^{dr+}) \right\} \Delta t \\ & \mathcal{N}_V \subseteq \mathcal{N}, \mathcal{N}_W \subseteq \mathcal{N}, \mathcal{N}_X \subseteq \mathcal{N} \end{aligned} \tag{14}$$

$$\begin{aligned} C_{w,t}^b & = \frac{1}{2} \frac{\left[C_{inv}^b + \sum_{i=1}^n C_{om}^b (1+dr)^{-i} \right] (1+dr)^n - RV}{(1+dr)^n \chi_T^\Xi \chi_T^\Upsilon \chi_d^\Upsilon \Upsilon_{w,ref} \Xi_{w,ref}} \\ & w \in \mathcal{N}_W, t \in \mathcal{T} \end{aligned} \tag{15}$$

5.2. Grid Connection Constraints

The maximum power, transferred between UG and microgrid, is restricted by grid-tie line capacity. It is represented by P_{max}^g and provided in (16). For maintenance of grid-tie line, scheduled islanding status is denoted by z_t to present DC MG operation in islanded mode, as described in (17). The $\neg z_t$ is logical negation of z_t.

$$0 \leq P_t^{g+}, P_t^{g-} \leq P_{max}^g (\neg z_t) \qquad t \in \mathcal{T} \tag{16}$$

$$z_t = \begin{cases} 1, & \text{if islanding} \\ 0, & \text{otherwise} \end{cases} \qquad t \in \mathcal{T} \tag{17}$$

5.3. PV System Constraints

The PV system output power is discussed in section III. It is well known that the power output of PV systems varies with irradiance and temperature. Therefore, equations (18) and (19) are modified to take into account the time t dependence of the generated power.

$$\begin{aligned} P_{v,t,av}^{pv} & = N_v^{pv} P_{STC}^{pv} \left[\frac{G_t}{G_{STC}} (1 - \gamma(T_{c,t} - T_{STC})) \right] \\ & v \in \mathcal{N}_V, t \in \mathcal{T} \end{aligned} \tag{18}$$

6

$$T_{c,t} = T_t + \frac{G_t}{G_{NOCT}}(NOCT - 20) \qquad t \in \mathcal{T} \qquad (19)$$

Power output of the PV system for each bus v should remain within the limit of the maximum available PV power $P_{v,t,av}^{pv}$.

$$0 \le P_{v,t}^{pv} \le P_{v,t,av}^{pv} \qquad v \in \mathcal{N}_V, t \in \mathcal{T} \qquad (20)$$

5.4. Li-ion Battery Constraints

Charging and discharging power of the Li-ion battery is controlled by the charging and discharging rate variables. The relations between these variables are provided by equations (21) and (22). These rates are restricted by the maximum limit defined in (23) and (24). Equation (25) ensures that battery should either charge or discharge at any time $t \in \mathcal{T}$, but not both simultaneously. Equation (26) defines intertemporal nature of battery, where its energy capacity changes with time t. In real time, DMO decides the final energy state of the battery according to the statistical analysis of the DC MG operation history. However, for this case study, it is assumed that initial and final state of energy capacity of the Li-ion battery should remain the same, as defined by (27). Equations (28) and (29) define maximum and minimum bounds on energy capacity of the Li-ion battery and the minimum energy capacity controlled by DOD at time t, respectively. Maximum energy capacity of the battery depends on temperature to consider power fading. However, temperature changes with time, thus changing maximum energy capacity of battery with time and making the proposed optimization problem intractable. Therefore, its average value, denoted by μ_T, is considered in calculating the maximum energy capacity in (30).

$$P_{w,t}^{ch} = R_{w,t}^{ch}\Xi_{w,ref} \qquad w \in \mathcal{N}_W, t \in \mathcal{T} \qquad (21)$$

$$P_{w,t}^{dch} = R_{w,t}^{dch}\Xi_{w,ref} \qquad w \in \mathcal{N}_W, t \in \mathcal{T} \qquad (22)$$

$$0 \le R_{w,t}^{ch} \le CR_{w,max} \qquad w \in \mathcal{N}_W, t \in \mathcal{T} \qquad (23)$$

$$0 \le R_{w,t}^{dch} \le DCR_{w,max} \qquad w \in \mathcal{N}_W, t \in \mathcal{T} \qquad (24)$$

$$R_{w,t}^{ch}R_{w,t}^{dch} = 0 \qquad w \in \mathcal{N}_W, t \in \mathcal{T} \qquad (25)$$

$$\Xi_{w,t} = \Xi_{w,t-1} + \left[\eta^{ch}P_{w,t}^{ch} - \frac{P_{w,t}^{dch}}{\eta^{dch}}\right]\Delta t \quad w \in \mathcal{N}_W, t \in \mathcal{T} \qquad (26)$$

$$\Xi_{w,t_f} = \Xi_{w,t_s} \qquad w \in \mathcal{N}_W \qquad (27)$$

$$\Xi_{w,min} \le \Xi_{w,t} \le \Xi_{w,max} \qquad w \in \mathcal{N}_W \qquad (28)$$

$$\Xi_{w,max} = \Xi_{ref}\chi_{\mu_T}^{\Xi} \qquad w \in \mathcal{N}_W \qquad (29)$$

$$\Xi_{w,min} = \Xi_{w,max}(1 - d) \qquad w \in \mathcal{N}_W \qquad (30)$$

5.5. DR Constraints

Equations (31) and (32) define the shifted load from time t and recovered load at time t, respectively. Equation (33) defines that DR load demand can be either shifted or recovered at time t, but both these processes cannot happen at the same time. Modified load demand after DR is presented in (34) and it cannot be more than the maximum value of the base load demand, which is controlled by (35). Equation (36) assures that the total recovered DR load must be equal to the shifted DR load. Shifted DR load from time t to i and total shifted DR load from t are constrained by the maximum shiftable DR load, as established by (37). All the defined variables are non-negative, as presented in (38).

$$P_{x,t}^{dr+} = \sum_{\substack{i \in \mathcal{T}_{sh} \\ i \ne t}} P_{x,t,i}^{dr} \qquad x \in \mathcal{N}_X, t \in \mathcal{T} \qquad (31)$$

$$P_{x,t}^{dr-} = \sum_{\substack{i \in \mathcal{T}_{sh} \\ i \ne t}} P_{x,i,t}^{dr} \qquad x \in \mathcal{N}_X, t \in \mathcal{T} \qquad (32)$$

$$P_{x,t}^{dr+}P_{x,t}^{dr-} = 0 \qquad x \in \mathcal{N}_X, t \in \mathcal{T} \qquad (33)$$

$$P_{x,t}^l = L_{x,t}^b - P_{x,t}^{dr+} + P_{x,t}^{dr-} \qquad x \in \mathcal{N}_X, t \in \mathcal{T} \qquad (34)$$

$$\sum_{x \in \mathcal{N}_X} P_{x,t}^l \le \| \sum_{x \in \mathcal{N}_X} L_{x,t}^b \|_\infty \qquad t \in \mathcal{T} \qquad (35)$$

$$\sum_{t=t_s}^{t_f} \sum_{x \in \mathcal{N}_X} P_{x,t}^{dr+} = \sum_{t=t_s}^{t_f} \sum_{x \in \mathcal{N}_X} P_{x,t}^{dr-} \qquad (36)$$

$$P_{x,t,i}^{dr}, P_{x,t}^{dr+} \le P_{x,t,max}^{dr} \qquad x \in \mathcal{N}_X, t \in \mathcal{T} \qquad (37)$$

$$P_{x,t}^{dr+}, P_{x,t}^{dr-} \ge 0 \qquad x \in \mathcal{N}_X, t \in \mathcal{T} \qquad (38)$$

5.6. Network Constraints

In a DC MG system, voltage of each bus should be considered and system losses have to be accounted while optimizing each generation source scheduling and DR. Otherwise, the proposed energy model cannot provide accurate results. Therefore, power flow constraints of the DC MG network are considered. Equation (39) is the power injection equation for bus i. Bus voltages are constrained by lower and upper bounds, as presented in (40). Line losses and total system losses at time t are given in (41) and (42), respectively.

$$P_t^i = \sum_{\substack{j=1 \\ j \ne i}}^{N} V_t^i(V_t^i - V_t^j)y_{ij} \qquad i \in \mathcal{N} \qquad (39)$$

$$V_{min}^i \le V_t^i \le V_{max}^i \qquad i \in \mathcal{N} \qquad (40)$$

$$P_{ij,t}^{loss} = (V_t^i - V_t^j)^2 y_{ij} \qquad j \ne i, (i,j) \in \mathcal{N}, t \in \mathcal{T} \qquad (41)$$

$$P_t^{loss} = \sum_{i=1}^{N-1} \sum_{j=i+1}^{N} P_{ij,t}^{loss} \qquad t \in \mathcal{T} \qquad (42)$$

5.7. Power Balance Constraint

Equation (43) ensures that the generated total power must be equal to the total demand, lost load, and system losses of the DC MG at each time t. $P_{x,t}^l$ relation is already given in (34).

$$(P_t^{g+} - P_t^{g-}) + \sum_{v \in \mathcal{N}_V} P_{v,t}^{pv} - \sum_{w \in \mathcal{N}_W} (P_{w,t}^{ch} - P_{w,t}^{dch})$$

$$= \sum_{x \in \mathcal{N}_X} (P_{x,t}^l - P_{x,t}^{ls}) + P_t^{loss} \qquad t \in \mathcal{T} \qquad (43)$$

6. Numerical Studies

Time of use (TOU) energy prices of buying electricity for summer and winter seasons are taken from the Ontario Energy Boa-rd [50]. The TOU rates are divided into three zones of off-peak, mid-peak, and on-peak hours. The TOU energy prices of selling electricity and DR incentive benefits are derived from TOU energy rates of buying electricity. The TOU energy prices of buying and selling eletricity are shown in Fig. 6. DR incentive benefits are given in Table 1. Value of the lost load is assumed to be 2 $/kWh. A PV system of 15 kW is considered in this study. The rated capacity of the Li-ion battery is 38.4 kWh. Charging and discharging efficiency of Li-ion battery are taken to be 0.9. Residual value is assumed to be 30% of capital cost at the end of the battery life. It is assumed that the battery is 70% charged before starting operation. Value of investment cost of the PV system for DC applications is taken from [51]. Capital cost of the Li-ion battery is obtained from [52]. Operation and maintenance costs of the PV system and the Li-ion battery are considered 22 $/kW-year and 20 $/kW-year, respectively. Degradation factor of the PV system is assumed to be 0.05% and the discount rate is considered as 5%. The hourly temperature profiles of Dammam and Brest regions, in July and December months, are shown in Fig. 7 [53] for 24h operation. These months are considered to take into account the effects of temperature on performance of the PV system and the Li-ion battery for summer and winter seasons, respectively. Figure 7 shows the modified hourly load profiles of 24h of Dammam and Brest regions during July and December [54, 55]. The hourly irradiances of these regions are taken from [56] for a period of 24h. Figure 7 also shows the power output of 15 kW$_p$ PV system. These load profiles and PV system are considered for a 6-bus system, shown in Fig. 8. The line data and base voltage of this 6-bus system are taken from [57]. The power demand at load buses 4, 5, and 6 are assumed to be 25%, 45%, and 30% of total load, respectively. The minimum and maximum limit on each bus voltage is 0.95 pu and 1.05 pu, respectively. The proposed nonlinear programming model is solved by the primal-dual interior point method with GEKKO package in Python [58, 59].

6.1. PV System Cost and Energy Output

Hot and cold weather climate regions are selected to assess the power output and LCOE of the PV system. Dammam, Saudi Arabia is considered for hot weather climate, while Brest, France is chosen for cold weather climate region. Temperature and irradiance data of these cities are taken from [53, 56]. The comparison of the PV system LCOE for these cities is carried out. LCOE and annual energy output of Dammam and Brest regions are shown in Fig. 9. The LCOE of PV system at Dammam and Brest regions are 0.067 $/kWh and 0.1 $/kWh, respectively. The main reason of a higher LCOE for the later region is low irradiance. The annual energy output of first year
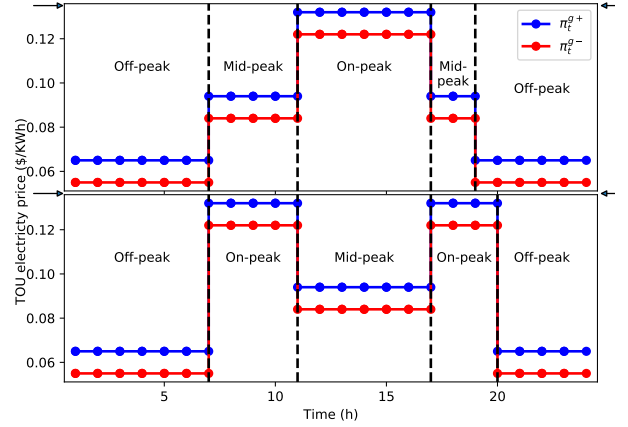

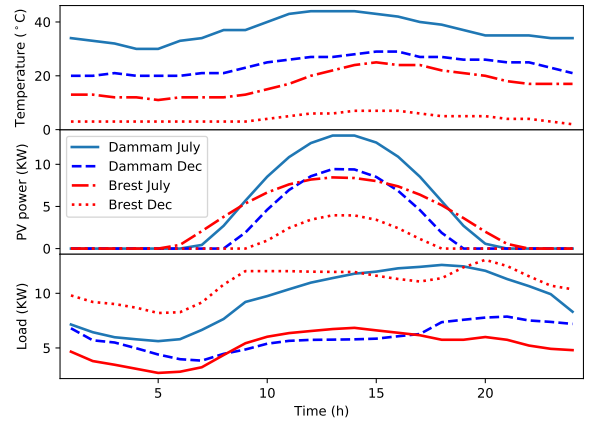Figure 6: TOU energy rates for summer (top) and winter (bottom).

Figure 7: Temperature profiles of Dammam and Brest regions (top), Power generation output of 15 kW$_p$ PV system for Dammam and Brest regions during December and July (mid), Load profiles of Dammam and Brest regions (bottom).
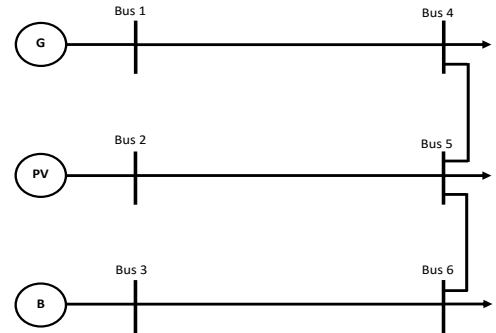

Figure 8: Single line diagram of 6-bus system.

of the PV system at Dammam and Brest regions is calculated to be 33.01 MWh and 22.05 MWh, respectively.

6.2. Impact of Temperature

The ideal operating temperature range, 10°C to 50°C, for a Li-ion battery operation is discussed in [60]. It shows that decreasing this temperature range leads to wasteful thermal management of the battery and increasing it leads to fast rise in the aging process. Temperature strongly affects discharged capac-

Table 1: Time-of-use DR incentive.

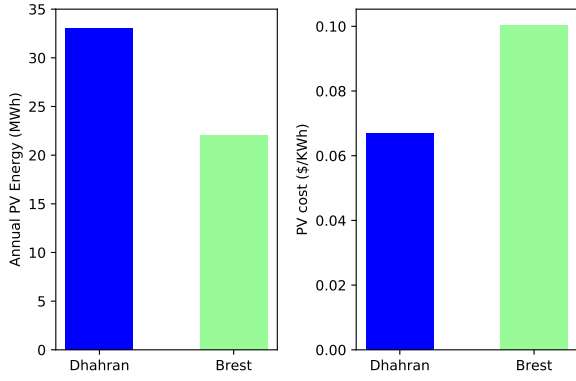|	Off-Peak	Mid-Peak	On-Peak
DR incentive (grid connected) [$/MWh]	0	5	10
DR incentive (scheduled islanding) [$/MWh]	10	10	10

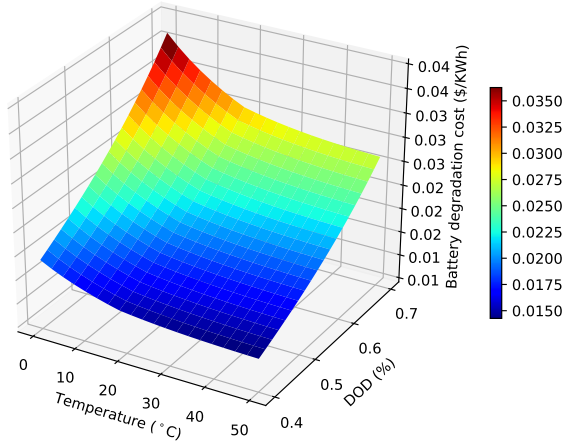Figure 9: Annual Energy output (left) and LCOE (right) of PV system.

Figure 10: Effects of temperature and DOD on Li-ion battery degradation cost.
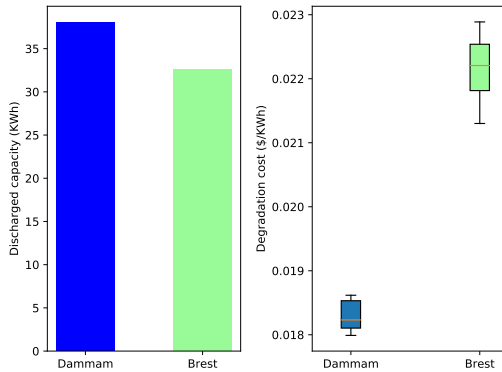

Figure 11: Maximum available discharged capacity (Left) and degradation cost variation (right) of Li-ion battery during 24h in December.

ity of BDC of the Li-ion battery. Figure 10 shows the change in the BDC with DOD and temperature. BDC strongly increases with the decrease in temperature below 10°C and increase in DOD. BDC cost analysis shows that a DOD of 0.6 and a temperature above 10°C provide lower cost for Li-ion battery operation.

As temperature depends on geographical locations, the BDC is therefore location-dependent. Therefore, two hot and cold climate regions are considered to study the Li-ion battery degradation. The discharged capacity and variation in BDC of the Li-ion battery during a 24h period in December is shown in Fig. 11. The discharged capacity of battery at Dammam is higher

Table 2: Impact of temperature on operating cost of DC MG without PV

	Trading Cost (pu)	Battery Cost (pu)	Total Cost (pu)
Dammam	0.947	0.053	1.0
Brest	0.957	0.054	1.011
Cost increase at Brest	0.01	0.001	0.011 (1.1%)

than Brest due to temperature differences of these regions. At Brest, low temperature causes reduction in available discharge capacity, thus rising the BDC cost. Moreover, the BDC variation at Brest is higher than Dammam.

The operating cost of the DC MG is also analyzed considering temperature dependence of the Li-ion battery degradation cost. For this purpose, a grid-connected DC MG without PV is considered for both Dammam and Brest winter cases. The same values of load demand are taken for this study. Results presented in Table 2 show an increase in the operating cost of the DC MG at Brest site due to lesser availability of discharge capacity and higher BDC. Hence, operating cost of the DC MG increases by 1.1% for 24h operation at Brest. These results show that the temperature considerably increases the operating cost of a DC MG system in cold weather regions. Therefore, a temperature-dependent BDC model of a Li-ion battery is more practical in deciding daily optimal scheduling of a DC MG system.

6.3. Brest and Dammam During Summer

In this case, the DC MG operation is studied for the cases of no DR, DR, and short period scheduled islanding in Brest and Dammam for 24h in July. Figures 12 and 13 show line losses, voltage profiles of buses, and optimal power scheduling for Brest and Dammam, respectively for 24h operation without DR. The system losses remain very low, below 0.08 kW during 24h period. Simulation results for Brest and Dammam with DR of 6h shift, line losses, voltage profiles of buses, load before and after DR, and dispatch for energy balance of the DC MG are given by Figs. 14 and 15, respectively. The 6h DR shift consists of 3h consecutive forward shift and 3h consecutive backward shift. The maximum shiftable load is assumed to be 10% of the total load at bus x and time t. These figures show that the load demand shifts from high energy price period, thus reducing the operating cost of the DC MG with the
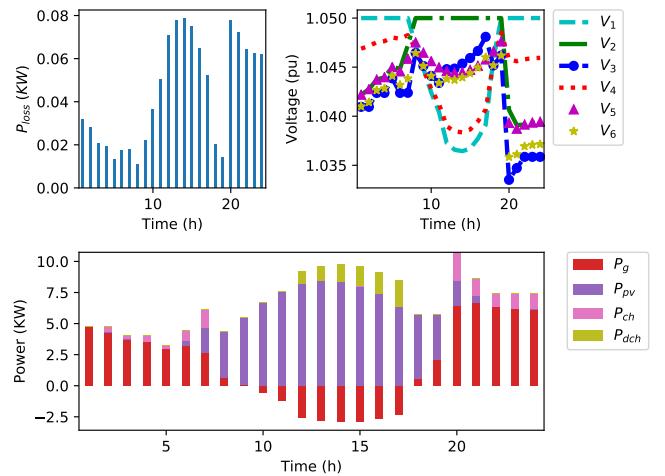

Figure 12: Power losses (top left), bus voltages (top right), and scheduling (bottom) of DC MG without DR at Brest in summer.
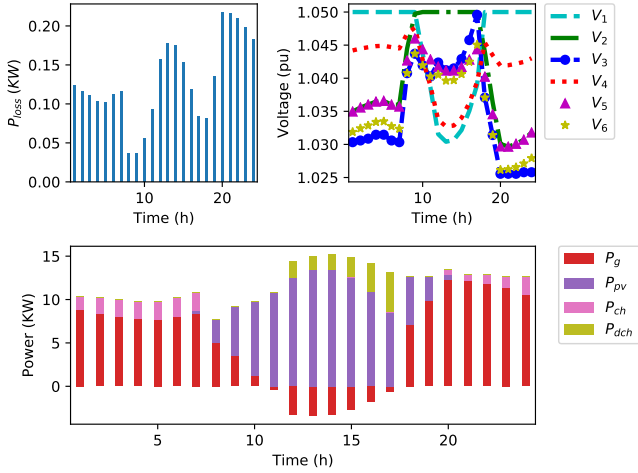
Figure 13: Power losses (top left), bus voltages (top right), and scheduling (bottom) of DC MG without DR at Dammam in summer.
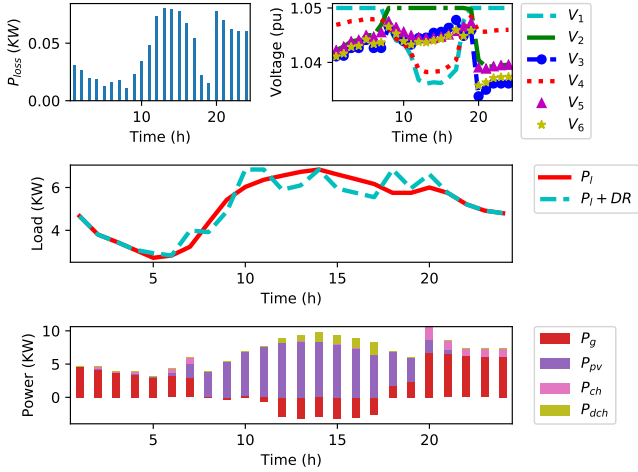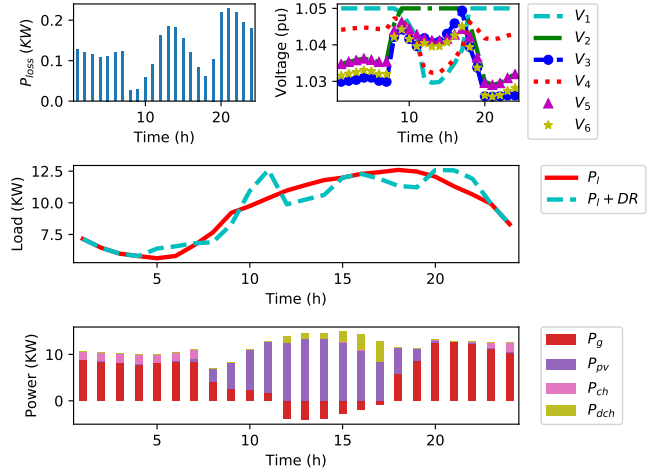

Figure 15: Power losses (top left), bus voltages (top right), load with DR (mid), and dispatch (bottom) for DC MG with DR at Dammam in summer.

Figure 14: Power losses (top left), bus voltages (top right), load with DR (mid), and dispatch (bottom) for DC MG with DR at Brest in summer.
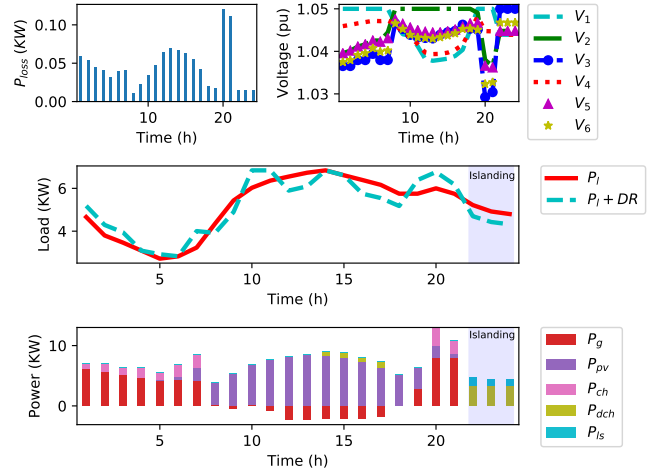

Figure 16: Power losses (top left), bus voltages (top right), load with DR (mid), and dispatch (bottom) for DC MG with DR and islanding at Brest in summer.

introduction of DR. In this study, the shiftable power consumption can be either increased or decreased at time instant t and 3h consecutive forward and backward shift duration are considered. Therefore, load at $t = 14h$ will not shift as load is being decreased at three time instants before and after it. Moreover, shiftable load moves to mid-peak periods due to the allowed 3h forward and backward shifts. However, in case of all-day shift, shiftable load shifts from on-peak energy price periods to off-peak energy periods, thus achieving the minimum DC MG operation cost. However, the DC MG cost reduces with increasing DR shift duration, which is shown in Table 3. For 10% of shiftable load, the DC MG cost reduces from 0.99 pu (1%) for 6h shift duration to 0.944 pu (5.6%) for all-day shift. For shiftable load equal to 20% of total load, the DC MG cost reduces from 0.985 pu (1.5%) for 6h shift to 0.912 pu (8.8%) for 10h shift. If shiftable load availability is 30% of total load, the DC MG cost reduces from 0.983 pu (1.7%) for 6h shift to 0.881 pu (11.9%) for all-day shift. No load shedding happens for normal operating conditions. Hence, the DMO should have a contract with consumers of all-day shift to achieve cost-effective DC MG operation and consumers will therefore receive incentives in return.

Considering scheduled maintenance of grid tie-line connection, islanding may happen for short interval of time during a 24h period. This case is also studied. Figures 16 and 17 show line losses, voltage profiles of buses, load before and after 6h shift DR, and dispatch for energy balance of the DC MG during islanding for Brest and Dammam, respectively. The Li-ion battery discharges during high price period and charges back to the maximum threshold to provide energy during the islanding period. Before islanding, battery charges at high rate and voltage of battery bus steeply decreases to around 1.03 pu, which results in higher system losses. Scheduled islanding is shown during the PV power absence periods. If islanding happens during excess PV power periods, the PV system will supply power to load buses, thus no load shedding will happen.

The operating cost comparison of the DC MG for different DR levels and DR duration periods for Brest is presented in Table 4. This table presents the cost comparison considering an

Table 3: Operating cost of DC MG without islanding for Brest in summer.

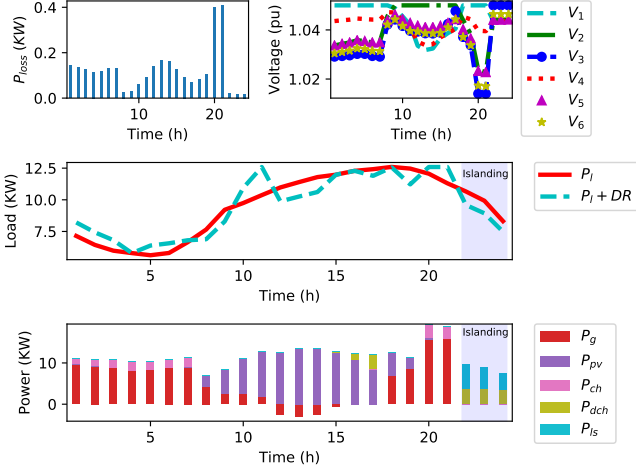| DR duration DR limit	No DR (pu)	6h (pu)	10h (pu)	23h (pu)
10% of $\sum_{x \in N_X} L^b_{x,t}$	1.0	0.990	0.957	0.944
20% of $\sum_{x \in N_X} L^b_{x,t}$	1.0	0.985	0.942	0.912
30% of $\sum_{x \in N_X} L^b_{x,t}$	1.0	0.983	0.932	0.881

Figure 17: Power losses (top left), bus voltages (top right), load with DR (mid), and dispatch (bottom) for DC MG with DR and islanding at Dammam in summer.

islanding period of 3h. As the islanding period is considered for 3h only, operating cost of the DC MG remains the same with respect to the demand shift period of 6h onwards, but it strongly decreases with the increase in DR shift value.

Table 5 provides the cost comparison of the DC MG for different DR values and DR shifting hours for Dammam region. For 6h shift, operating cost of the DC MG decreases by 1.1%, 1.6%, 1.9% for DR of 10%, 20%, and 30% of the base load, respectively. However, it noticeably decreases with the increase in DR time shift for the same values of the shifted load. Similarly, Table 6 presents the cost comparison considering an islanding period of 3h. This table shows that the operating cost decreases with the increase in the value of the shifted load.

6.4. Brest and Dammam During Winter

In this case, the DC MG operation at Brest and Dammam in December is studied for the cases of no DR, DR, and short period scheduled islanding of 3h. Figures 18 and 19 show line losses, voltage profiles of buses, and optimal power scheduling at Brest and Dammam, respectively, for 24h operation without DR. At Brest, due to battery charging and high load demand, load and battery bus voltages decreases sharply and produces maximum line losses of 0.31 kW. Optimization results with DR

Table 4: Operating cost of DC MG with islanding for Brest in summer.

DR limit	DR duration			
	No DR (pu)	6h (pu)	10h (pu)	23h (pu)
10% of $\sum_{x \in N_X} L_{x,t}^b$	1.0	0.858	0.845	0.838
20% of $\sum_{x \in N_X} L_{x,t}^b$	1.0	0.720	0.704	0.685
30% of $\sum_{x \in N_X} L_{x,t}^b$	1.0	0.584	0.564	0.533

Table 5: Operating cost of DC MG without islanding for Dammam in summer.

DR limit	DR duration			
	No DR (pu)	6h (pu)	10h (pu)	23h (pu)
10% of $\sum_{x \in N_X} L_{x,t}^b$	1.0	0.989	0.964	0.950
20% of $\sum_{x \in N_X} L_{x,t}^b$	1.0	0.984	0.951	0.911
30% of $\sum_{x \in N_X} L_{x,t}^b$	1.0	0.981	0.941	0.873

Table 6: Operating cost of DC MG with islanding for Dammam in summer.

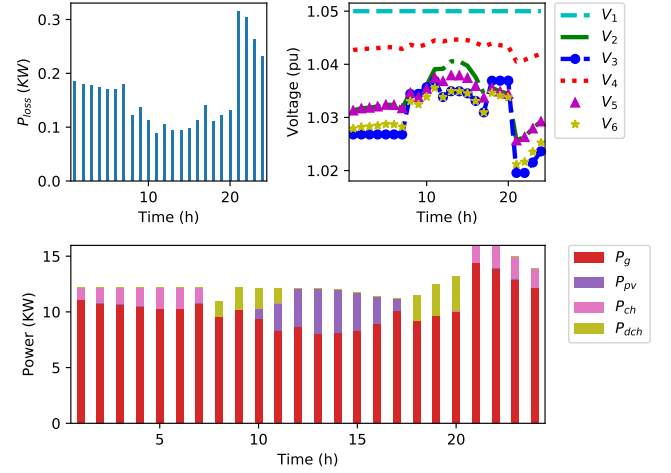| DR limit	DR duration			
	No DR (pu)	6h (pu)	10h (pu)	23h (pu)
10% of $\sum_{x \in N_X} L_{x,t}^b$	1.0	0.889	0.885	0.877
20% of $\sum_{x \in N_X} L_{x,t}^b$	1.0	0.780	0.774	0.757
30% of $\sum_{x \in N_X} L_{x,t}^b$	1.0	0.671	0.663	0.657

Figure 18: Power losses (top left), bus voltages (top right), and scheduling (bottom) of DC MG without DR at Brest in winter.
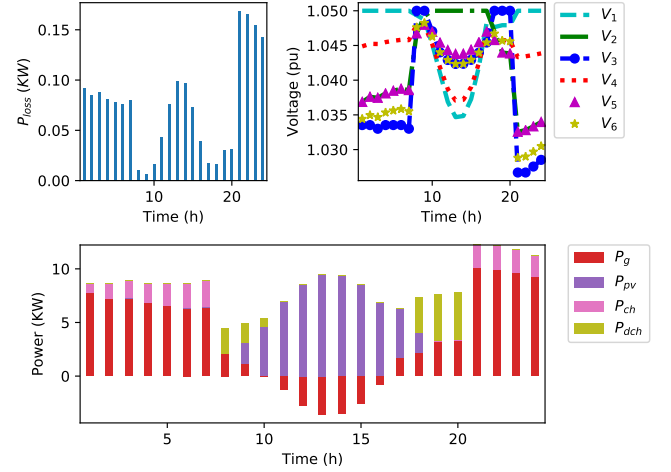

Figure 19: Power losses (top left), bus voltages (top right), and scheduling (bottom) of DC MG without DR at Dammam in winter.

of 6h shift are given by Figs. 20 and 21 for Brest and Dammam regions, respectively. DR load is shifted to mid-peak price periods as 3h forward and backward shifts are considered. However, with the increase in DR shift duration, the shiftable load moves to off-peak price periods, thus reducing the DC MG operation cost effectively. There is no load shedding in normal operation.

Figures 22 and 23 show line losses, voltage profiles of buses, and optimal power scheduling at Brest and Dammam, respectively, for 24h operation in December for a 3h scheduled islanding period with a DR of 6h shift. These figures show that the battery charges at a high c-rate just one hour before islanding. At this time, the battery bus voltage decreases sharply to just below 1.0 pu and increases line losses.

The operating cost comparison of the DC MG at Brest for different DR levels and DR duration periods is presented in Table 7. This table shows that operating cost of the DC MG is decreasing with the increase of the demand shift period and the DR shift limit. For 6h DR shift, on-peak instants load can be shifted to mid-peak price periods only, thus reducing cost by only 1.8%, 2.2%, and 3.1% for a shiftable load of 10%, 20%, and 30% of the total load, respectively. However, the shiftable
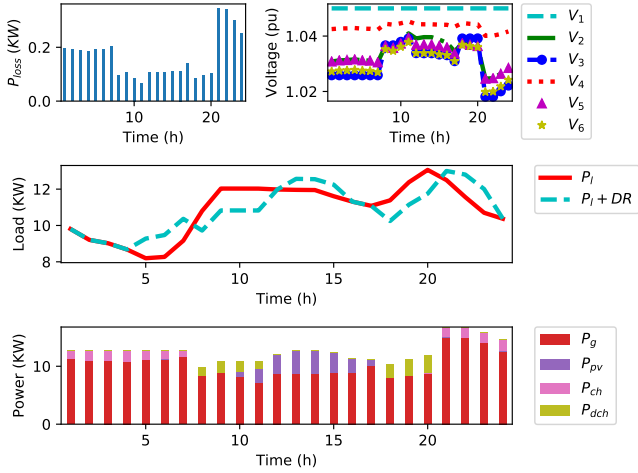
Figure 20: Power losses (top left), bus voltages (top right), load with DR (mid), and dispatch (bottom) for DC MG with DR at Brest in winter.
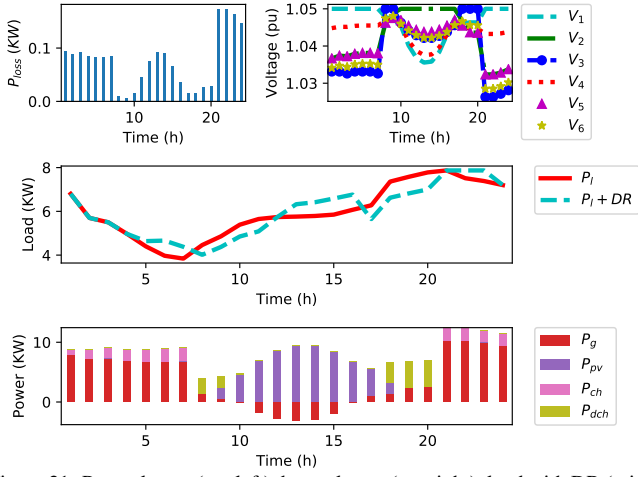

Figure 21: Power losses (top left), bus voltages (top right), load with DR (mid), and dispatch (bottom) for DC MG with DR at Dammam in winter.
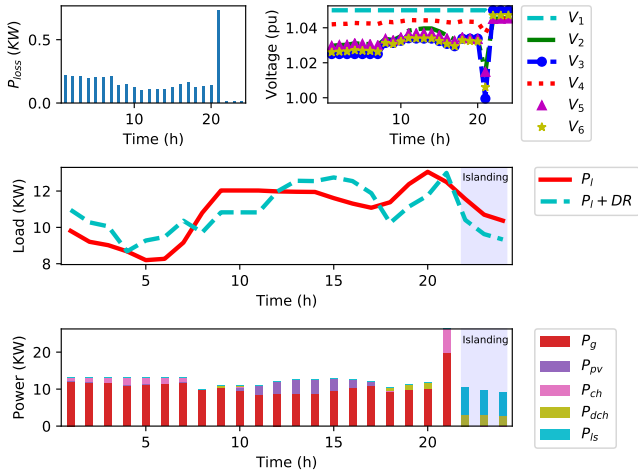

Figure 22: Power losses (top left), bus voltages (top right), load with DR (mid), and dispatch (bottom) for DC MG with DR and islanding at Brest in winter.

load moves to off-peak price periods in all-day shift duration, thus resulting in higher cost reduction of 4.3%, 6.0%, and 8.0% for a shiftable load of 10%, 20%, and 30% of the total load, respectively. Similarly, Table 8 presents the cost comparison considering an islanding period of 3h. As the islanding period
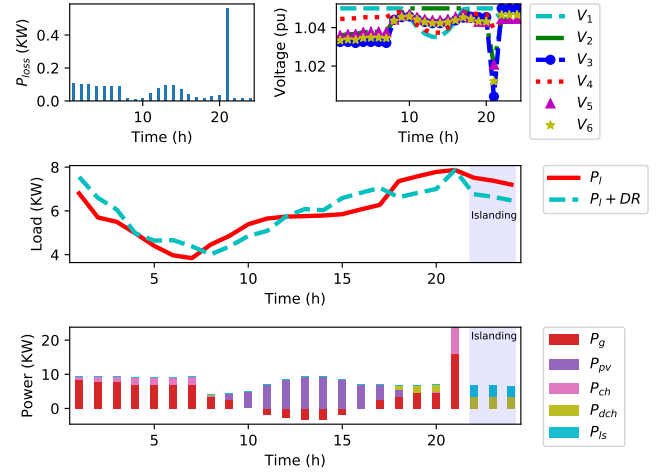

Figure 23: Power losses (top left), bus voltages (top right), load with DR (mid), and dispatch (bottom) for DC MG with DR and islanding at Dammam in winter.

is considered for 3h only, therefore operating cost of the DC MG remains the same with respect to the demand shift period of 6h onwards, but it remarkably decreases with the increase in DR shifting values with respect to the base load.

Table 9 refers to operating cost of the DC MG at Dammam for different DR values and DR shift periods in terms of base load. This table clearly shows that the operating cost of the DC MG is decreasing with the increase of the demand shift and the DR shift limit. Similarly, Table 10 presents the cost comparison considering an islanding period of 3h. Operating cost considerably decreases for 6h shift period by 32.9% for 30% shiftable demand of the base load. It cannot decrease more due to the maximum limit on recovered demand that can be shifted at any time t. However, it decreases by 39% and 39.8% for 10h and 23h period for the same amount of shiftable demand.

Table 7: Operating cost of DC MG without islanding for Brest in winter.

DR duration DR limit	No DR (pu)	6h (pu)	10h (pu)	23h (pu)
10% of $\sum_{x \in \mathcal{N}_X} L^b_{x,t}$	1.0	0.982	0.978	0.969
20% of $\sum_{x \in \mathcal{N}_X} L^b_{x,t}$	1.0	0.968	0.957	0.938
30% of $\sum_{x \in \mathcal{N}_X} L^b_{x,t}$	1.0	0.957	0.940	0.920

Table 8: Operating cost of DC MG with islanding for Brest in winter.

DR duration DR limit	No DR (pu)	6h (pu)	10h (pu)	23h (pu)
10% of $\sum_{x \in \mathcal{N}_X} L^b_{x,t}$	1.0	0.907	0.906	0.901
20% of $\sum_{x \in \mathcal{N}_X} L^b_{x,t}$	1.0	0.816	0.815	0.806
30% of $\sum_{x \in \mathcal{N}_X} L^b_{x,t}$	1.0	0.725	0.719	0.715

Table 9: Operating cost of DC MG without islanding for Dammam in winter.

DR duration DR limit	No DR (pu)	6h (pu)	10h (pu)	23h (pu)
10% of $\sum_{x \in \mathcal{N}_X} L^b_{x,t}$	1.0	0.982	0.964	0.952
20% of $\sum_{x \in \mathcal{N}_X} L^b_{x,t}$	1.0	0.967	0.946	0.918
30% of $\sum_{x \in \mathcal{N}_X} L^b_{x,t}$	1.0	0.953	0.929	0.890

Table 10: Operating cost of DC MG with islanding for Dammam in winter.

DR duration DR limit	No DR (pu)	6h (pu)	10h (pu)	23h (pu)
10% of $\sum_{x \in \mathcal{N}_X} L^b_{x,t}$	1.0	0.872	0.867	0.862
20% of $\sum_{x \in \mathcal{N}_X} L^b_{x,t}$	1.0	0.752	0.738	0.728
30% of $\sum_{x \in \mathcal{N}_X} L^b_{x,t}$	1.0	0.671	0.61	0.602

6.5. Real World Applications

In energy management operation of the DC MG, decision strategies and informations are exchanged between local controllers and the DC MG operator using communication links. In DC MGs, such as rural, residential, and remote areas microgrids, communication technologies are decided on the basis of data rate and infrastructure cost. ZigBee, Wi-Fi, and Z-Wave are more suitable options. Low cost embedded systems, like Arduino, STM32, Rasberry Pi, and BeagleBone, can be adopted by local controllers to collect information and perform neccessay control actions. The DC MG operator is a human-to-machine system that performs energy management operation with the help of local controllers and a SCADA platform. The developed energy management model makes decision strategies with the information from all external factors and energy sources. It can be integrated in microgrid energy management modules, which are currently being developed by many energy companies as Schneider Electric, ABB, EDF, ENGIE, Alstom, Siemens, Tesla, and so forth, for optimal and efficient operation of microgrids. Hence, the developed model can be used for economic operation of a DC MG in the future.

7. Conclusion

In this paper, an optimization model was developed to minimize the operating cost of a DC microgrid. The proposed model includes aging factors-dependent practical degradation cost model of a Li-ion battery using real data. This model can be generalized to other types of batteries as they depict almost the same behavior. The optimization model also includes islanding-dependent demand response incentive to encourage active participation of customers during scheduled maintenance of grid-tie line. Levelized cost of photovoltaic system was also calculated using real data to obtain accurate cost for hot and cold climate regions. System losses and nodal voltages were also studied, as they are imperative in achieving realistic and efficient operation of a DC microgrid. Results analysis proves that, introducing islanding responsive demand response incentive and increasing the value of the shifted load demand and the demand response shift duration, greatly reduces the operating cost of the DC microgrid. Finally, temperature effects on operating cost of the DC microgrid without a photovoltaic system were analyzed. They show higher cost for cold climate region due to increased power fading of a Li-ion battery at low temperature. The obtained results confirmed that the integration of battery degradation cost and islanding responsive demand response incentives in DC microgrid applications would significantly influence the operating cost.

References

[1] M. F. Zia, E. Elbouchikhi, M. Benbouzid, Microgrids energy management systems: A critical review on methods, solutions, and prospects, Applied Energy 222 (2018) 1033–1055.

[2] M. Stadler, G. Cardoso, S. Mashayekh, T. Forget, N. DeForest, A. Agarwal, A. Schönbein, Value streams in microgrids: A literature review, Applied Energy 162 (2016) 980–989.

[3] D. Kumar, F. Zare, A. Ghosh, Dc microgrid technology: system architectures, ac grid interfaces, grounding schemes, power quality, communication networks, applications and standardizations aspects, IEEE Access 5 (2017) 12230–12256.

[4] C. Wang, J. Yan, C. Marnay, N. Djilali, E. Dahlquist, J. Wu, H. Jia, Distributed energy and microgrids (DEM), Applied Energy 210 (2018) 685–689.

[5] E. Bullich-Massagué, F. Díaz-González, M. Aragüés-Peñalba, F. Girbau-Llistuella, P. Olivella-Rosell, A. Sumper, Microgrid clustering architectures, Applied Energy 212 (2018) 340–361.

[6] P. Wu, W. Huang, N. Tai, S. Liang, A novel design of architecture and control for multiple microgrids with hybrid AC/DC connection, Applied Energy 210 (2018) 1002–1016.

[7] D. Boroyevich, I. Cvetković, D. Dong, R. Burgos, F. Wang, F. Lee, Future electronic power distribution systems a contemplative view, in: 12th International Conference onOptimization of Electrical and Electronic Equipment (OPTIM), IEEE, 2010, pp. 1369–1380.

[8] L. Herrera, W. Zhang, J. Wang, Stability analysis and controller design of dc microgrids with constant power loads., IEEE Transactions on Smart Grid 8 (2) (2017) 881–888.

[9] T. Dragičević, X. Lu, J. C. Vasquez, J. M. Guerrero, Dc microgrids–part i: A review of control strategies and stabilization techniques, IEEE Transactions on Power Electronics 31 (7) (2016) 4876–4891.

[10] M. Aneke, M. Wang, Energy storage technologies and real life applications–a state of the art review, Applied Energy 179 (2016) 350–377.

[11] P. Sanjeev, N. P. Padhy, P. Agarwal, Peak energy management using renewable integrated dc microgrid, IEEE Transactions on Smart Grid 9 (5) (2018) 4906–4917.

[12] K. Chaudhari, A. Ukil, K. N. Kumar, U. Manandhar, S. K. Kollimalla, Hybrid optimization for economic deployment of ess in pv-integrated ev charging stations, IEEE Transactions on Industrial Informatics 14 (1) (2018) 106–116.

[13] M. O. Badawy, Y. Sozer, Power flow management of a grid tied pv-battery system for electric vehicles charging, IEEE Transactions on Industry Applications 53 (2) (2017) 1347–1357.

[14] S. Chalise, J. Sternhagen, T. M. Hansen, R. Tonkoski, Energy management of remote microgrids considering battery lifetime, The Electricity Journal 29 (6) (2016) 1–10.

[15] C. Bordin, H. O. Anuta, A. Crossland, I. L. Gutierrez, C. J. Dent, D. Vigo, A linear programming approach for battery degradation analysis and optimization in offgrid power systems with solar energy integration, Renewable Energy 101 (2017) 417–430.

[16] W. Su, J. Wang, J. Roh, Stochastic energy scheduling in microgrids with intermittent renewable energy resources, IEEE Transactions on Smart Grid 5 (4) (2014) 1876–1883.

[17] Y. Zhang, A. Lundblad, P. E. Campana, F. Benavente, J. Yan, Battery sizing and rule-based operation of grid-connected photovoltaic-battery system: A case study in sweden, Energy Conversion and Management 133 (2017) 249–263.

[18] J. Cai, H. Zhang, X. Jin, Aging-aware predictive control of PV-battery assets in buildings, Applied Energy 236 (2019) 478–488.

[19] G. Cardoso, T. Brouhard, N. DeForest, D. Wang, M. Heleno, L. Kotzur, Battery aging in multi-energy microgrid design using mixed integer linear programming, Applied Energy 231 (2018) 1059–1069.

[20] T. A. Nguyen, M. L. Crow, Stochastic optimization of renewable-based microgrid operation incorporating battery operating cost, IEEE Transactions on Power Systems 31 (3) (2016) 2289–2296.

[21] P. Cicconi, D. Landi, M. Germani, Thermal analysis and simulation of a li-ion battery pack for a lightweight commercial EV, Applied Energy 192 (2017) 159–177.

[22] J. Spector, Lithium-ion storage installs could grow 55% every year through 2022, Tech. rep., Greentech Media, Massachusetts, United States (2018).

[23] M. Jin, W. Feng, P. Liu, C. Marnay, C. Spanos, MOD-DR: Microgrid optimal dispatch with demand response, Applied Energy 187 (2017) 758–776.

[24] C. Gu, X. Yan, Z. Yan, F. Li, Dynamic pricing for responsive demand to increase distribution network efficiency, Applied Energy 205 (2017) 236–243.

[25] D. Yu, H. liu, C. Bresser, Peak load management based on hybrid power

generation and demand response, Energy 163 (2018) 969–985.

[26] J. Anjo, D. Neves, C. Silva, A. Shivakumar, M. Howells, Modeling the long-term impact of demand response in energy planning: The portuguese electric system case study, Energy 165 (2018) 456–468.

[27] A. Mohsenzadeh, C. Pang, M.-R. Haghifam, Determining optimal forming of flexible microgrids in the presence of demand response in smart distribution systems, IEEE Systems Journal 12 (4) (2018) 3315–3323.

[28] J. Wang, H. Zhong, Z. Ma, Q. Xia, C. Kang, Review and prospect of integrated demand response in the multi-energy system, Applied Energy 202 (2017) 772–782.

[29] P. Siano, Demand response and smart grids – a survey, Renewable and Sustainable Energy Reviews 30 (2014) 461–478.

[30] Y. Gong, Y. Cai, Y. Guo, Y. Fang, A privacy-preserving scheme for incentive-based demand response in the smart grid, IEEE Transactions on Smart Grid 7 (3) (2016) 1304–1313.

[31] Z. Zhou, M. Benbouzid, J. F. Charpentier, F. Scuiller, T. Tang, A review of energy storage technologies for marine current energy systems, Renewable and Sustainable Energy Reviews 18 (2013) 390–400.

[32] B. Stiaszny, J. C. Ziegler, E. E. Krauß, M. Zhang, J. P. Schmidt, E. Ivers-Tiffée, Electrochemical characterization and post-mortem analysis of aged limn2o4–nmc/graphite lithium ion batteries part ii: Calendar aging, Journal of Power Sources 258 (2014) 61–75.

[33] E. Sarasketa-Zabala, E. Martinez-Laserna, M. Berecibar, I. Gandiaga, L. Rodriguez-Martinez, I. Villarreal, Realistic lifetime prediction approach for li-ion batteries, Applied energy 162 (2016) 839–852.

[34] C. Zhou, K. Qian, M. Allan, W. Zhou, Modeling of the cost of ev battery wear due to v2g application in power systems, IEEE Transactions on Energy Conversion 26 (4) (2011) 1041–1050.

[35] Lithium—Smart LiFePO$_4$, Victron Energy, JG Almere Haven , Netherland.

[36] ION Power Battery Pack—40290203, Whisper Power, JB Drachten, Netherland.

[37] A. Zeh, M. Müller, M. Naumann, H. C. Hesse, A. Jossen, R. Witzmann, Fundamentals of using battery energy storage systems to provide primary control reserves in germany, Batteries 2 (3) (2016) 29.

[38] L. Lam, P. Bauer, Practical capacity fading model for li-ion battery cells in electric vehicles, IEEE Transactions on Power Electronics 28 (12) (2013) 5910–5918.

[39] A. Cordoba-Arenas, S. Onori, Y. Guezennec, G. Rizzoni, Capacity and power fade cycle-life model for plug-in hybrid electric vehicle lithium-ion battery cells containing blended spinel and layered-oxide positive electrodes, Journal of Power Sources 278 (2015) 473–483.

[40] G. Sarre, P. Blanchard, M. Broussely, Aging of lithium-ion batteries, Journal of Power Sources 127 (1-2) (2004) 65–71.

[41] J. Vetter, P. Novák, M. R. Wagner, C. Veit, K.-C. Möller, J. Besenhard, M. Winter, M. Wohlfahrt-Mehrens, C. Vogler, A. Hammouche, Ageing mechanisms in lithium-ion batteries, Journal of Power Sources 147 (1-2) (2005) 269–281.

[42] V. Agubra, J. Fergus, Lithium ion battery anode aging mechanisms, Materials 6 (4) (2013) 1310–1325.

[43] I. Bloom, B. Cole, J. Sohn, S. Jones, E. Polzin, V. Battaglia, G. Henriksen, C. Motloch, R. Richardson, T. Unkelhaeuser, D. Ingersoll, H. Case, An accelerated calendar and cycle life study of li-ion cells, Journal of Power Sources 101 (2) (2001) 238–247.

[44] J. Hall, A. Schoen, P. Allen, P. Liu, K. Kirby, Resistance growth in lithium ion satellite cells. i. non destructive data analyses, in: 208th ECS Meeting, The Electrochemical Society, 2005, pp. 242–242.

[45] C. S. Park, Fundamentals of engineering economics, Pearson/Prentice Hall (Upper Saddle River, NJ), 2004.

[46] IRENA, Renewable capacity statistics 2018, Tech. rep., International Renewable Energy Agency (IRENA), Abu Dhabi (2018).

[47] A. Luque, S. Hegedus, Handbook of photovoltaic science and engineering, John Wiley & Sons, 2011.

[48] K. Branker, M. Pathak, J. M. Pearce, A review of solar photovoltaic levelized cost of electricity, Renewable and Sustainable Energy Reviews 15 (9) (2011) 4470–4482.

[49] A. Skoczek, T. Sample, E. D. Dunlop, The results of performance measurements of field-aged crystalline silicon photovoltaic modules, Progress in Photovoltaics: Research and applications 17 (4) (2009) 227–240.

[50] Time of use rate – Ontario Energy Board, (accessed on 2018-10-20).
URL https://www.oeb.ca/rates-and-your-bill/
electricity-rates/managing-costs-time-use-rates

[51] R. Fu, D. J. Feldman, R. M. Margolis, M. A. Woodhouse, K. B. Ardani, Us solar photovoltaic system cost benchmark: Q1 2017, Tech. rep., National Renewable Energy Lab.(NREL), Golden, CO (United States) (2017).

[52] N. Kittner, F. Lill, D. M. Kammen, Energy storage deployment and innovation for the clean energy transition, Nature Energy 2 (9) (2017) 17125.

[53] Temperature data, (accessed on 2018-10-20).
URL https://www.wunderground.com

[54] I. El Amin, M. F. Zia, M. Shafiullah, Selecting energy storage systems with wind power in distribution network, in: IECON 2016-42nd Annual Conference of the IEEE Industrial Electronics Society, IEEE, 2016, pp. 4229–4234.

[55] O. H. Mohammed, Y. Amirat, M. Benbouzid, G. Feld, T. Tang, A. Elbast, Optimal design of a stand-alone hybrid pv/fuel cell power system for the city of brest in france, International Journal on Energy Conversion 2 (1) (2014) 1–7.

[56] Irradiance data, (accessed on 2018-10-20).
URL http://www.solarelectricityhandbook.com/
solar-irradiance.html

[57] C. Li, S. K. Chaudhary, M. Savaghebi, J. C. Vasquez, J. M. Guerrero, Power flow analysis for low-voltage ac and dc microgrids considering droop control and virtual impedance, IEEE Transactions on Smart Grid 8 (6) (2017) 2754–2764.

[58] L. Beal, D. Hill, R. Martin, J. Hedengren, Gekko optimization suite, Processes 6 (8) (2018) 106.

[59] A. Wächter, L. T. Biegler, On the implementation of an interior-point filter line-search algorithm for large-scale nonlinear programming, Mathematical programming 106 (1) (2006) 25–57.

[60] N. Kim, A. Rousseau, Electric drive vehicle level control development under various thermal conditions: 2012 DOE hydrogen program and vehicle technologies annual merit review, Tech. rep., Department of Energy, Virginia, US (2012).